Magnetic Phase Transitions and Magnetoelastic Coupling in a Two-Dimensional Stripy Antiferromagnet

Pingfan Gu,[●] Yujia Sun,[●] Cong Wang,[●] Yuxuan Peng, Yaozheng Zhu, Xing Cheng, Kai Yuan, Chao Lyu, Xuelu Liu, Qinghai Tan, Qinghua Zhang, Lin Gu, Zhi Wang, Hanwen Wang, Zheng Han,[*] Kenji Watanabe, Takashi Taniguchi, Jinbo Yang, Jun Zhang,[*] Wei Ji,[*] Ping-Heng Tan, and Yu Ye[*]

Read Online

ACCESS | Metrics & More | Article Recommendations | SI Supporting Information

ABSTRACT: Materials with a quasi-one-dimensional stripy magnetic order often exhibit low crystal and magnetic symmetries, thus allowing the presence of various energy coupling terms and giving rise to macroscopic interplay between spin, charge, and phonon. In this work, we performed optical, electrical and magnetic characterizations combined with first-principles calculations on a van der Waals antiferromagnetic insulator chromium oxychloride (CrOCl). We detected the subtle phase transition behaviors of exfoliated CrOCl under varying temperature and magnetic field and clarified its controversial spin structures. We found that the antiferromagnetism and its air stability persist down to few-layer samples, making it a promising candidate for future 2D spintronic devices. Additionally, we verified the magnetoelastic coupling effect in CrOCl, allowing for the potential manipulation of the magnetic states via electric field or strain. These virtues of CrOCl provide us with an ideal platform for fundamental research on spin-charge, spin-phonon coupling, and spin-interactions.

KEYWORDS: 2D magnetic materials, stripy antiferromagnetism, magnetoelastic coupling, tunneling magnetoresistance
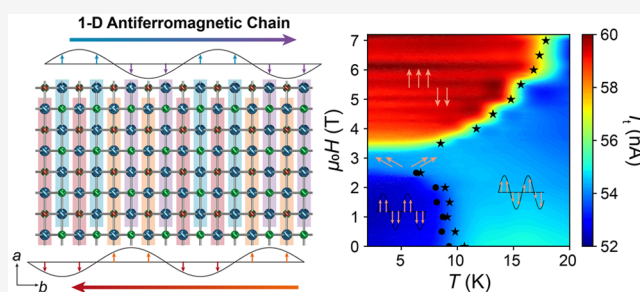
INTRODUCTION

Since the discovery of Peierls instability and charge density wave ground state,[1] one-dimensional (1D) crystals have been receiving lasting research interest. A series of fantastic physical properties were realized in 1D or quasi-1D magnetic materials thereafter, such as the spin density wave (SDW),[2] spin Peierls effect,[3] and improper magnetic ferroelectricity.[4] As 1D systems are strongly bonded in only one direction, they are sensitive to perturbations in three-dimensional space and result in structural instabilities and degeneracy breaking. Moreover, the electronic and magnetic ground states of a 1D system usually exhibit wave orders with low symmetry, allowing for various coupled energy terms. Generally, crystals composed of strong exchange-coupled spin chains isolated from each other can be regarded as quasi-1D spin systems.[5−7]

We can expect the 1D magnetic order, stripy antiferromagnetism, to be present in van der Waals (vdW) materials at the two-dimensional (2D) limit as the complex competition between the external field, thermal excitation and spin-exchange coupling in a 2D magnet will give rise to a variety of spin configurations beyond the conventional pictures. Coupling the quasi-1D spin chains with the atomic thickness not only allows us to tune the magnetic ground states by means of the electric field, free carrier doping or strain, but also provide us with an ideal platform to study spin-charge coupling and spin-phonon coupling.

CrOCl has recently been reported as a promising air-stable vdW antiferromagnetic (AFM) insulator.[8,9] The neutron scattering studies[10−14] describe the magnetic ground state of CrOCl as an unconventional SDW along the b-axis with an easy axis of the c-axis, that is, a stripy-y AFM order. As the temperature decreases, CrOCl first transforms from a paramagnetic state into an incommensurate SDW state at ∼27 K (T_{mag}), then into a commensurate state with an SDW wavelength of $4b$ (b is the lattice constant) at the Néel temperature of ∼14 K. Both neutron scattering[13,14] and X-ray diffraction (XRD)[15] results show that the magnetic phase transition at Néel temperature is accompanied by a structural phase transition from orthorhombic space group $Pmmn$ to monoclinic space group $P2_1/m$, indicating sizable magnetoelastic coupling in CrOCl.

Despite the above studies, there are still many remaining questions regarding this complicated material, which are of great significance for revealing the basic mechanism of 3d
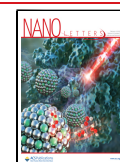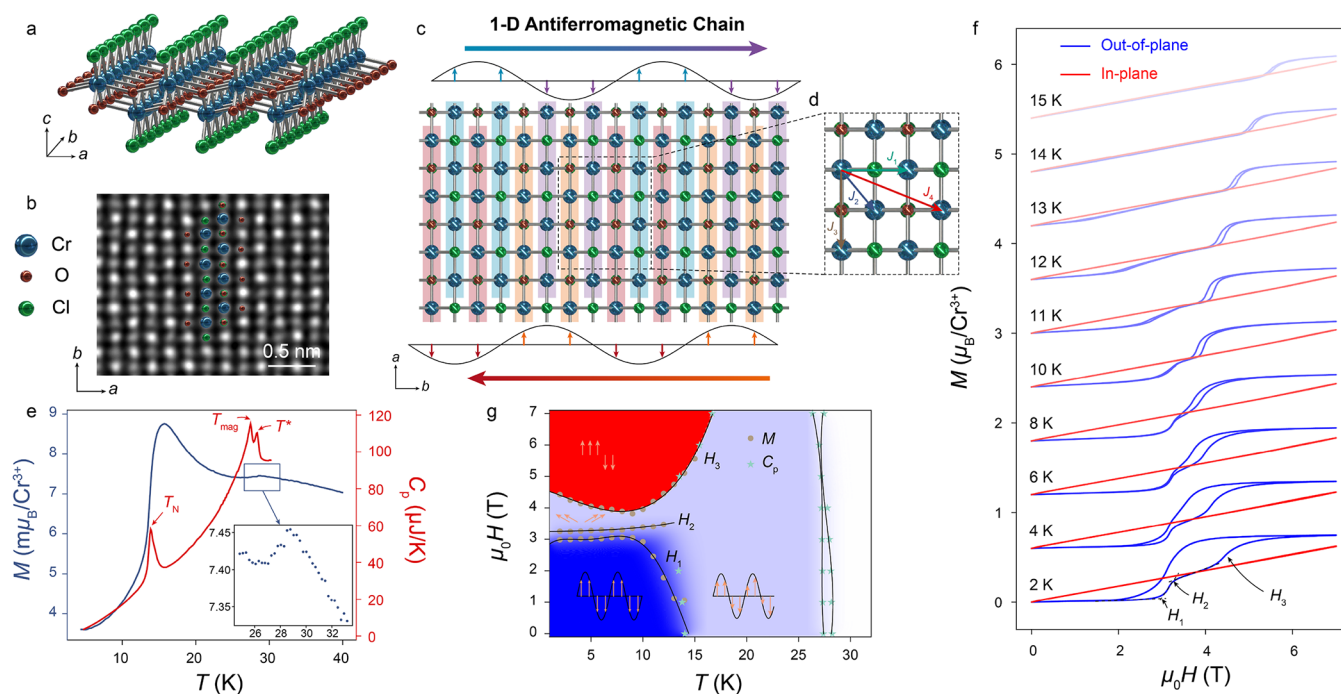
Figure 1. Basic characterizations and phase transition behaviors of CrOCl. (a) The atomic structure of single-layer CrOCl. (b) Atomic resolution high-angle annular dark-field STEM (HAADF-STEM) image viewed from the [001] direction. The atoms of a single magnetic unit cell are labeled by the spherical models. (c) The low-temperature magnetic structure of CrOCl in the commensurate phase. The upper and lower wave displays the AFM chains along the b-axis in two sublayers with a phase shift of π. The stripe-ordered magnetic structure is superimposed on the atomic structure. The blue and purple regions correspond to the Cr moment pointing up or down in the upper sublayer, while the red and orange regions correspond to that of the lower sublayer. (d) The magnetic exchange interaction of first (J_1), second (J_2), third (J_3), and fourth (J_4) nearest neighbor. (e) Magnetic moment (blue left axis) and heat capacity (red right axis) of the bulk CrOCl on the dependence of temperature. The transition temperatures are annotated by T^*, T_{mag}, and T_N. The inset shows the magnetic moment peak near T^* and T_{mag}. (f) $M-H$ curves with the applied field parallel or perpendicular to the c-axis at different temperatures. Each curve is vertically shifted by 0.6 μ_B/Cr^{3+} from the lower one. H_1 and H_2 marks the beginning and the end of the spin-flop transition obtained by linear fitting of different slopes in $M-H$ curve, and H_3 labels the second transition to the ↑↑↑↓↓ phase, which was obtained from the maximum of the first derivative of the $M-H$ curve. Only the H-up diagram was demonstrated for clear identification of the transition lines. (g) Phase diagram of bulk CrOCl crystal. The phase boundaries are extracted from the heat capacity and magnetization measurements. The spin configurations of each phase are illustrated by golden arrows.

electron interactions and determining the possible spintronic applications of CrOCl. For example, distinct from other 2D antiferromagnets,[16,17] several unconventional magnetic phase transitions are detected under varying external field,[13,15] but the magnetic order of each phase remains unclear. Additionally, the magnetic properties of few-layer samples are also unknown. These issues have been receiving increasing interest recently and have been studied through theoretical calculations.[18−26] However, due to the complexity of the three filled 3d orbitals, some calculation results are contradictory.

Here, we verified the magnetoelastic coupling effect in exfoliated CrOCl by Raman spectroscopy and investigated the magnetism of few-layer CrOCl by tunneling magnetoresistance. Combining the characterization results with first-principle calculations, we uncovered the multistep magnetic phase transitions under the external field along the easy axis down to 2D limit. We also analyzed the detailed behavior of each transition, which reflects the accompanying structural changes due to magnetoelastic coupling. Our findings not only advance the understanding of this unexplored promising material but also reveal the rich physics and potential for spintronic devices of magnetoelastic materials.

■ RESULTS AND DISCUSSION

We synthesized CrOCl single crystals via the chemical vapor transport (CVT) method (see Methods). The crystal structure

of CrOCl consists of two Cr−O sublayers sandwiched between the Cl atom layers stacked along the c-axis (Figure 1a). Thanks to its stability, scanning transmission electron microscopy (STEM) is used to reveal the atomic ordering of exfoliated CrOCl (Figure 1b). The brighter contrast of Cr columns over Cl/O columns can be identified, matching well with the simulated results (Figure S1). Energy dispersive spectroscopy (EDS) and electron energy loss spectroscopy (EELS) are also performed to verify the composition of the crystal (Figure S1 and Table S1).

The CrOCl crystal changes from an orthorhombic phase at room temperature to a monoclinic phase below the Néel temperature due to magnetoelastic coupling and exhibits an sAFM-↑↑↓↓ magnetic ground state.[13−15] The sAFM-↑↑↓↓ ground state (Figure 1c) is verified by density functional theory (DFT) calculations (Supporting Information (SI) Note S1, Figure S2, and Table S2) and proved to be robust to changes in the on-site Coulomb energy U value in a reasonable range below 3.9 eV (Figure S3). A ferrimagnetic-like ↑↑↑↓↓ state (FiM2-↑↑↑↓↓) is found to be metastable with an energy difference ($E_{↑↑↑↓↓} - E_{↑↑↓↓}$) of 1.0 meV/Cr (Figure S2 and Table S2). The origin of this behavior can be traced by the derived spin exchange parameters $J_1 = -0.26$ meV, $J_2 = -0.89$ meV, $J_3 = 1.29$ meV, and $J_4 = 0.44$ meV Figure 1d. The large positive J_3 leads to an ferromagnetic (FM) coupled stripe along the a-axis, and the competition between J_1, J_2, and J_4 gives rise
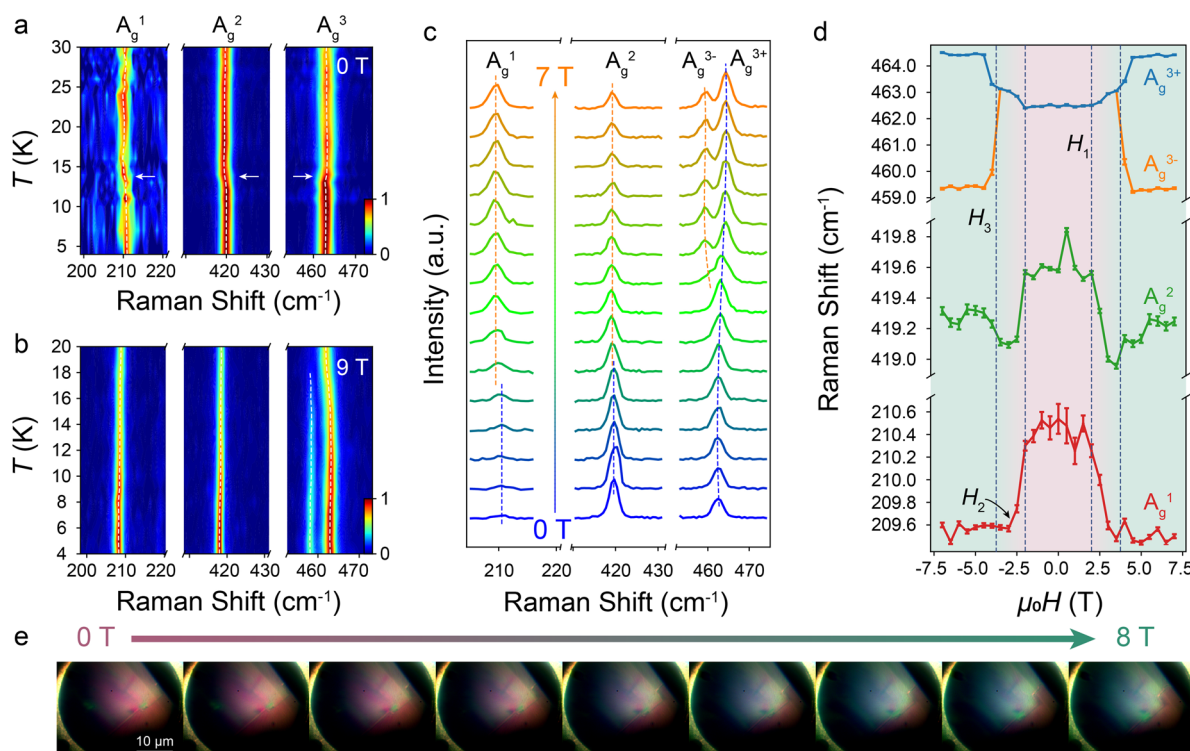
Figure 2. Optical characterizations of the exfoliated CrOCl. (a,b) Raman spectra of CrOCl as a function of temperature under an external field of 0 T (a) and 9 T (b). The intensities of the three peaks are normalized and the colorbars are shown in the lower right insets. The white arrows indicate the frequency shift of the peaks at the Néel temperature. The dashed white lines track the evolution of the peak frequencies. (c) Raman spectra of CrOCl on the dependence of the external field at 4 K. (d) The extracted peak frequencies of panel c. The shaded areas indicate the ↑↑↓↓ phase, the ↑↑↑↓↓ phase, and the intermediate phases (including the spin-flop phase and the canting phase) between them. The transition fields H_1, H_2, and H_3 are labeled by the dashed lines or arrow. (e) Optical micrographs of an exfoliated CrOCl under external fields.

to the favored sAFM-↑↑↓↓ order (Figure 1d and Table S4). According to the calculated band structure, the energy dispersion along k_y is ultraflat, being a possible factor in the unique ground state along the b-axis (Figure S4).

To visualize the low-temperature phase transitions, we measured the temperature-dependent magnetic moment and heat capacity of bulk CrOCl, where a magnetic field $\mu_0 H = 0.1$ T was applied along the c-axis (Figure 1e). An ambiguous peak of magnetic moment and two heat capacity peaks at ∼28.0 K indicate the appearance of the incommensurate state, which is a pure magnetic transition. The magnetic moment increases following the paramagnetic law in the incommensurate state due to the weak coupling between the stripes until the Néel temperature at ∼14.0 K, where the magnetic moment decreases rapidly, and another heat capacity peak appears, manifesting in the formation of the robust AFM state. Noticeably, as we measure the heat capacity around the Néel temperature, the sample temperature rise shows obvious relaxation process (Figure S5), which can be attributed to the latent heat of the first-order transition.[27]

To clearly observe the evolution of the magnetic states, we measured the magnetic moment with varying magnetic fields parallel or perpendicular to the easy axis under different temperatures (Figure 1f). At the lowest temperature (2 K) with $H∥c$, the zero net magnetization platform persists to ∼3 T, and then undergoes two successive jumps to reach another plateau. A large hysteresis loop appears when the applied field sweeps back to zero. The first magnetic transition marks the collapse of the AFM order and disappears above the Néel temperature, while the second transition exists but shifts to a

higher field. After the first magnetic transition under the out-of-plane magnetic field, the net moment jumps to the magnetization value under the same in-plane field and begins to rise analogously, so we attribute it to a typical spin-flop transition. Meanwhile, the net moment of the plateau after the second phase transition is ∼0.6 μ_B/Cr³⁺, one-fifth of the saturation magnetic moment of Cr³⁺, suggesting the appearance of a stable colinear state, the ↑↑↑↓↓ state, revealed by our DFT calculations (Table S2). The calculated energy difference between the ↑↑↓↓ and ↑↑↑↓↓ states is 1.0 meV/Cr³⁺, that is, 5.8 T, close to the observed second transition field. We note that the broadening and hysteresis behaviors of the two transitions also evidence the first-order nature and magnetoelastic coupling of CrOCl (see Figure S7 and followed discussion). On the basis of the $M-H$ curves, we constructed the phase diagram of bulk CrOCl with magnetic field and temperature (Figure 1g). H_1 and H_2 mark the start and end of the spin-flop transition obtained by linear fitting of different slopes in $M-H$ curves, and H_3 marks the second transition to the ↑↑↑↓↓ phase, which was obtained from the maximum of the first derivative of the $M-H$ curves. The peak positions of heat capacity are also marked and coincide with the phase boundaries.

After understanding the transition behaviors of bulk CrOCl, the next question is whether the antiferromagnetism and the magnetoelastic coupling persist to the exfoliated samples. We first examined an exfoliated CrOCl by magnetic force microscopy (MFM) at 2 K (Figure S6). A significant phase difference between the nanoflake and substrate at 6 T confirms that the AFM order is still present. Additionally, the two most
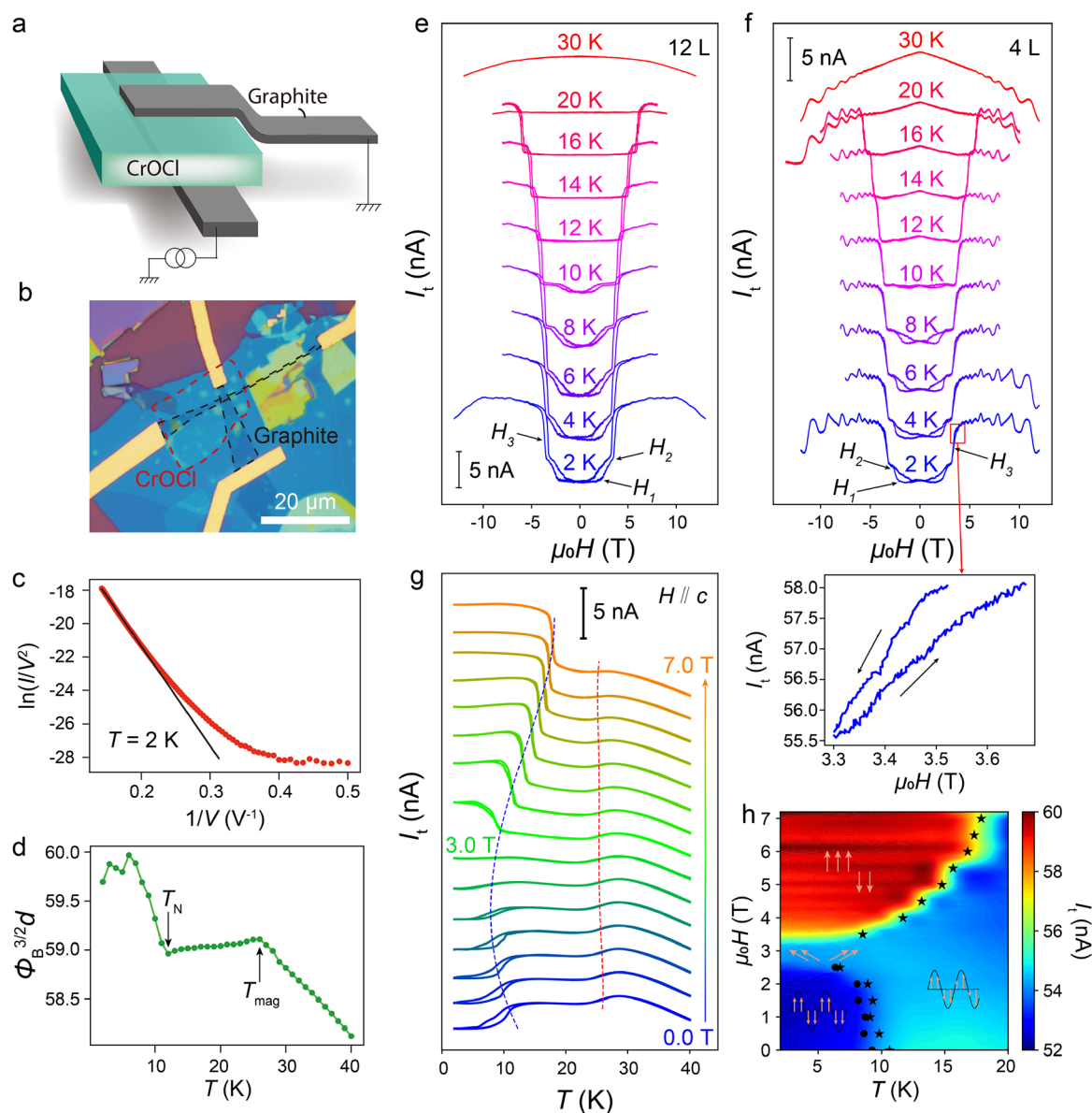
Figure 3. Tunneling magnetoresistance measurements of exfoliated CrOCl thin flakes. (a) Cartoon illustration of the tunneling device. (b) Optical image of a tunneling device. The CrOCl flake and graphite stripes are highlighted by red and black dashed lines, respectively. The tunneling junction is encapsulated by hBN. (c) The measured $\ln\frac{I}{V^2}$ versus $1/V$ at 2 K. The black line shows linear fitting result at a high voltage range. (d) The extracted $\phi_B^{3/2}d$ by fitting the $I-V$ curves at different temperatures. The transition temperatures are annotated by T_{mag} and T_N. (e,f) The measured tunneling current versus out-of-plane external field curves at different temperatures of a 12-L (e) and a 4-L (f) tunneling sample. Each curve is vertically shifted by 6 nA (e) and 5 nA (f) from the lower one. The lower inset in (f) illustrates the hysteresis loop of the transition from the spin-canting phase to the ↑↑↑↓↓ phase measured at 2 K. (g) The $I-T$ curves at different external fields. Each curve is vertically shifted by 2.5 nA from the lower one. The red dashed line indicates the transition from the paramagnetic phase to the incommensurate phase, while the blue dashed line indicates the transition from the incommensurate phase to the ↑↑↓↓ at low fields and to the ↑↑↑↓↓ phase at high fields. (h) Color plot of the tunneling current as a function of out-of-plane magnetic field and temperature. The black spheres and stars mark the transition temperatures extracted from the downward and upward scans in (g). The spin configuration of each phase is illustrated by golden arrows.

common manifestations of magnetoelastic effect, magnetostriction and the lowering of the crystal symmetry, will affect the lattice vibration modes. As a result, we measured the Raman spectra of the exfoliated sample to reveal the magnetoelastic coupling effect.

The Raman spectra consist of three main A_g modes located near 210 cm^{-1} (A_g^1), 419 cm^{-1} (A_g^2), and 462 cm^{-1} (A_g^3), the Raman tensor of which are verified via polarized Raman spectroscopy (Figure S8). Although the $P2_1/m$ group consists of 12 representative A_g modes,[28] no additional peaks were

observed below the Néel temperature, possibly due to their weak electron−phonon coupling. Below the Néel temperature, all three peaks show apparent frequency shifts (Figure 2a, where A_g^1 and A_g^2 modes blue-shift, while A_g^3 red-shifts), and the intensities of A_g^2 and A_g^3 are clearly enhanced (Figure S9). Similar effects caused by spin−lattice coupling have been reported in other 3d-electron magnetic systems.[29−33] The three calculated characteristic A_g peaks in the ↑↑↓↓ state are consistent with the experimental observations, with frequency differences less than 2% (Figure S10). The calculated Raman
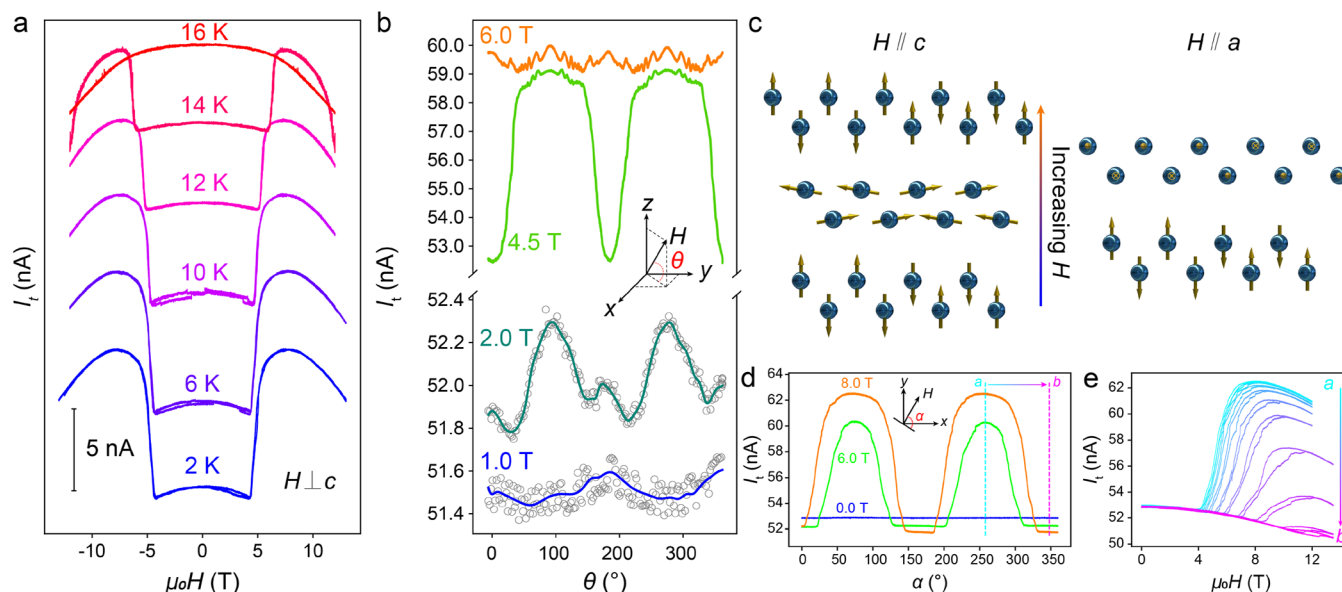
Figure 4. In-plane anisotropic response of the 4-L tunneling device. (a) Tunneling current versus in-plane field at different temperatures. Each curve is vertically shifted by 5 nA from the lower one. (b) Angle-dependent tunneling current under different external fields. The external field rotated along an in-plane axis to the c-axis. θ is the angle between the external field and the in-plane axis. (c) Illustration of the in-plane and out-of-plane magnetic transitions of CrOCl. (d) The tunneling current on the dependence of the in-plane field direction at different external fields. (e) Tunneling current versus in-plane field as the field points toward different in-plane directions. The transition field gradually increases as external field deviates from the a-axis.

tensor matrix elements are also consistent with the experimental results from the polarized Raman measurements (Figure S11, Figure S12, Table S5, and Table S6). The vibration displacements revealed by DFT show that the A_g^1 and A_g^2 modes correspond to the intralayer breathing mode within each sublayer vibrating along the c-direction, suggesting their phonon energies should be highly sensitive to a sudden change of lattice constant along the c-axis, but less affected by in-plane distortions. In contrast, the A_g^3 mode contains relative vibrations between each two adjacent magnetic stripes along the a-axis through inequivalent O atoms (Figure S13). As a result, A_g^3 exhibits an opposite frequency shift upon structural phase transition and possibly reflects the change of magnetic unit cell.

For more information on the structural changes upon magnetic phase transitions, we measured temperature-dependent Raman spectra under a 9 T external field along the c-axis (Figure 2b). The most salient feature is that A_g^3 splits into two peaks below 19 K (A_g^{3-} and A_g^{3+}), corresponding to the transition from the incommensurate phase to the ↑↑↑↓↓ phase. No distinct changes of A_g^1 and A_g^2 were observed, implying transition free from the sudden change of layer thickness. At 4 K as the external field increases, the splitting of the A_g^3 mode occurs at 4 T (Figure 2c,d), which approximately agrees with the H_3 value of the bulk sample (Figure 1f). Our calculations also show that, relative to the ↑↑↓↓ ground state, the A_g^3 mode splits into A_g^{3-} and A_g^{3+} in the FiM2-↑↑↑↓↓ state (Figure S10 and Figure S14). These two split peaks exhibit identical anisotropic pattern in the polarized Raman measurements, consistent with our calculation results (Figure S11 and Figure S12). Meanwhile, the spin-flop transition can also be detected in the field-dependent Raman spectra (Figure 2c), where three Raman modes show exactly the same energy shifts in the zero-field heating process (Figure 2d and discussion in SI Note S2), confirming the sudden decrease of layer thickness.[13] Uniquely,

changes in band structure and thus the refractive index are magnified upon the magnetic and structural transitions, leading to a significant magnetochromism effect in the crystal (Figure 2e).

In addition to Raman spectroscopy, tunneling magnetoresistance is another sensitive probe to detect the magnetic phase transitions for ultrathin magnets[16,34] (SI Note S3). We contacted few-layer CrOCl (4-SL and 12-SL, Figure S16) with cross-structured few-layer graphene strips (see Methods) to measure the tunneling magnetoresistance of CrOCl (Figure 3a,b). For the case of the 12-L CrOCl, insulating behavior was observed at low voltages and on-current was measurable over 4 V, where the Fowler–Nordheim (FN) tunneling model applies,[35,36] described as[37]

$$\ln \frac{I}{V^2} \sim -\frac{8\pi\sqrt{2m^*}\phi_B^{3/2}d}{3heV} \qquad (1)$$

As we can see, at voltages larger than the CrOCl bandgap, that is, $1/V < 0.4\ V^{-1}$, the experimental data $\ln\frac{I}{V^2}$ versus $1/V$ exhibit an overt linear relationship (Figure 3c). Consequently, the combined value of $\phi_B^{3/2}d$ can be determined by fitting the $I-V$ curves at different temperatures (Figure 3d). The two transition temperatures, T_N and T_{mag}, can be clearly detected and the detailed information on magnetic and structural changes are discussed in SI Note S3. The Néel temperature here is ~12 K, slightly lower than that of bulk crystal, possibly due to the enhanced thermal fluctuations of the exfoliated samples.

Figure 3e,f compares the tunneling current versus out-of-plane field curves at different temperatures of the 12-L (Figure 3e) and the 4-L (Figure 3f) sample. Magnetic phase transitions are detected in both samples, and the transition fields H_1, H_2, and H_3 are labeled by black arrows. The depression of the tunneling current in both samples at low field, signifying the

existence of AFM state, disappears at ∼12 K, which is consistent with the predicted Néel temperature in Figure 3d. The magnetoelastic coupling effect and the resulted metastable states in the 2D limit are also manifested as distinct hysteresis loops (inset of Figure 3f and discussions following Figure S7). The persistence of AFM order in the 2D limit can further be verified in the $I-T$ curves of the 4-L sample (Figure 3g). The temperature-dependent resistance tendency of the 4-L sample is slightly different from the 12-L sample (Figure 3d) due to the thermal expansion effect and interfacial effect in the 2D limit (discussed in Figure S17). At fields lower than 3 T, CrOCl enters the sAFM-↑↑↓↓ state below the Néel temperature (∼10 K), manifested as a decrease in tunneling current and a large hysteresis loop. Above 3 T, CrOCl enters the ↑↑↑↓↓ state at low temperatures (marked by the blue dashed line), manifested as a sharp increase in tunneling current and a subtle hysteresis. Using the data in Figure 3h, we constructed the 4-L CrOCl magnetic phase diagram in which the downward and upward transition temperatures extracted from the $I-T$ curves (marked by the black spheres and stars) are consistent with the phase boundaries. The evolution of the different magnetic states precisely accord with the bulk phase diagram (Figure 1d).

Surprisingly, when the external field is applied along an in-plane axis, we observed another unexpected phase transition in all measured samples (Figure 4a and Figure S20). The transition exhibits a nearly constant transition field at different temperatures and persists above 12 K, slightly higher than the Néel temperature. When the external field is rotated in the ab-plane of the sample, the tunneling current shows an exactly 180° periodic symmetry (Figure 4d), implying the C_2 in-plane symmetry of CrOCl. When the field points to the a-axis, the tunneling currents jump at ∼5.5 T, while points to the b-axis, the transition can hardly occur (Figure 4e and Figure S18). Apparently, the common two-sublattice AFM model containing quadratic anisotropic exchange interactions and single-ion anisotropy energy cannot cause such a magnetic phase transition (Figure S7). More complicated higher-order energy terms must be introduced.

Physically speaking, there are two explanations for such a transition under the in-plane magnetic field: the in-plane projection of the spins in the ground state is nonzero, or the magnetoelastic coupling energy drives the system into a more energetically favorable state (e.g., in-plane ↑↑↑↓↓ state). Our phenomenological model rules out the possibility that the ground state Néel vector points in the ac-plane (Figure S19 and followed discussion). Furthermore, when the external field was rotated from an in-plane axis to the c-axis (Figure 4b and Figure S20c), the tunneling current shows a 180° periodic symmetry (Table S7). This indicates that the ground state Néel vector points to the crystal axis, within the measurement uncertainty. Our DFT calculations also confirmed that the c-axis is the easy axis (Table S3), while the single-ion anisotropy energy makes the a-axis the secondary easy axis, and the b-axis the hardest magnetization axis. Actually, analogy to the second transition in the $H\|c$ configuration in which the external field perpendicular to the Néel vector drives the system into the colinear ↑↑↑↓↓ phase, it is reasonable to infer that the magnetic order here is also ↑↑↑↓↓ with spins pointing toward the a-axis, as illustrated in Figure 4c. The detailed magnetic and crystal structures are worthy of further investigation by neutron scattering under an applied field.

The remarkable in-plane anisotropic magnetic field response is compelling evidence for the stripy antiferromagnetic order of CrOCl. Moreover, the strong magnetic anisotropy may further explain the stiffness of the magnetism down to 2D limit. Reviewing the characterization of all CrOCl samples, we conclude that the exfoliation process and few-layer flakes of this vdW material do not have a substantial effects on its magnetism (Figure S21), except for the slightly enhanced thermal fluctuations and interfacial effects. This is probably because the AFM order of CrOCl is determined by the rigid intralayer exchange interactions, and the strong anisotropy helps to open a sizable magnon bandgap and stabilizes the 2D magnetic order. The persistence of magnetic order in the 2D limit, together with the good air stability and rich physics in CrOCl, will open the doors both toward fundamental research and AFM spintronics.

■ METHODS

Crystal Synthesis and Characterizations. A mixture of powdered $CrCl_3$ and Cr_2O_3 with a molar ratio of 1:1 and a total mass of 1.5 g were sealed in an evacuated quartz ampule. The ampule was then placed in a two-zone furnace, where the source and sink temperatures for the growth were set to 940 and 800 °C, respectively, and kept for 2 weeks. Subsequently, the furnace was slowly cooled to room temperature, and high-quality CrOCl crystals were obtained. Heat capacity and magnetization measurements were performed by standard modules of a Quantum Design PPMS. Because of the weak vdW coupling between adjacent layers, CrOCl crystals can be easily exfoliated down to few-layer flakes by the typical "Scotch Tape" method. The nanoflakes also exhibit remarkable stability and undergo no degeneration in air, so all the basic characterizations like AFM measurements, Raman measurements, and the device fabrication process of CrOCl are conducted in air (Figure S22).

Device Fabrication. Multilayer graphene, hBN (10−30 nm) and CrOCl flakes were exfoliated by the "Scotch Tape" method in ambient conditions. The heterostructures were then assembled with a conventional pick-up and release technique based on polypropylene carbonate (PPC)/polydimethylsiloxane (PDMS) polymer stacks placed on glass slides. Once encapsulated, the devices were annealed in a high vacuum with a flow of mixed H_2 and Ar to remove the residual PPC. Then the electron-beam lithography, reactive ion etching (in a plasma of a CHF_3/O_2 mixture), electron beam evaporation and lift-off were then used to define metal electrode contacts of 5/35 nm Cr/Au.

Raman Measurements. Raman spectra were measured using a Jobin-Yvon HR evolution system equipped with a liquid-nitrogen-cooled charge-coupled detector (CCD). A high numerical aperture (0.82) objective and 1800 grooves/mm grating were used in the Raman measurements. The excitation wavelength was 477 nm from an Ar^+ laser. The low-temperature and magnetic field were provided by an Attocube closed-cycle cryostat (attoDRY 1100). The angular-resolved polarized Raman spectra under parallel and perpendicular configurations were measured by rotating the half-wave plate in the common optical path of incident laser and scattered Raman signal to simultaneously change their polarization directions.

Electrical Measurements. Transport measurements were performed in a Heliox ^{3}He insert system equipped with a 14 T superconducting magnet. The lowest temperature of the

system is 1.8 K. To measure the $I-V$ characteristics of the tunnel barrier and their magnetoresistance, the bias voltage was applied using a Keithley 2636B source meter and the tunneling current was measured using the standard two-probe module. In order to obtain intrinsic signals and exclude any possibilities of Joule heating effect at the same time, the tunneling current is restricted to ∼50 nA such that the total power is merely ∼0.3 μW in a junction of ∼1 μm^2.

First-Principles Calculations. Our DFT calculations were performed using the generalized gradient approximation for the exchange-correlation potential. To exclude the influence of different structure on energy calculations, the energy differences between different magnetic configurations were calculated with same structure at the two limits, that is, using the optimized structures with FM and sAFM-↑↑↓↓ orders in a 1 × 20 × 1 supercell, respectively. The shape and volume of each supercell with different magnetic configurations (FM and sAFM-↑↑↓↓) were fully optimized and all atoms in the supercell were allowed to relax until the residual force per atom was less than 1×10^{-3} eV·Å^{-1}. More calculation details are presented in SI Note S1.

■ ASSOCIATED CONTENT

Ⓢ Supporting Information

The Supporting Information is available free of charge at https://pubs.acs.org/doi/10.1021/acs.nanolett.1c04373.

> Structural and chemical analysis of CrOCl, details of DFT calculation methods, calculated total energy of different spin configurations, calculated parameters of exchange interactions and anisotropy of the magnetic ground state, calculated band structure of different magnetic states, heat capacity measurement results, MFM measurement results, derivation of spin-flop transition, discussion on hysteresis and broadening behaviors of each transition, polarized Raman spectra and extracted Raman tensor elements, temperature-dependent Raman spectra, calculated Raman tensor and frequencies, illustrations of lattice vibrational modes, fitting results of field-dependent Raman, discussion on the spin-canting phases, discussion on the mechanism of tunneling magnetoresistance, AFM image of tunneling CrOCl samples, temperature-dependent resistivity behavior of tunneling devices, in-plane anisotropic magnetoresistance, theoretical model of spin-flop transitions in two directions, extracted anisotropic axes of the tunneling devices, extracted transition fields, study on air stability of CrOCl (PDF)

■ AUTHOR INFORMATION

Corresponding Authors

Zheng Han − *State Key Laboratory of Quantum Optics and Quantum Optics Devices, Institute of Optoelectronics, Shanxi University, Taiyuan 03006, China; Collaborative Innovation Center of Extreme Optics, Shanxi University, Taiyuan 03006, China;* Email: zhenghan@sxu.edu.cn

Jun Zhang − *State Key Laboratory of Superlattices and Microstructures, Institute of Semiconductors, Chinese Academy of Sciences, Beijing 100083, China; Center of Materials Science and Optoelectronics Engineering, University of Chinese Academy of Sciences, Beijing 100049, China;* ⓘ orcid.org/0000-0002-9831-6796; Email: zhangjwill@semi.ac.cn

Wei Ji − *Department of Physics and Beijing Key Laboratory of Optoelectronic Functional Materials and Micro-Nano Devices, Renmin University of China, Beijing 100872, China;* ⓘ orcid.org/0000-0001-5249-6624; Email: wji@ruc.edu.cn

Yu Ye − *State Key Laboratory for Mesoscopic Physics, Nano-optoelectronics Frontier Center of the Ministry of Education, School of Physics, Peking University, Beijing 100871, China; Collaborative Innovation Center of Quantum Matter, Beijing 100871, China; Yangtze Delta Institute of Optoelectronics, Peking University, Nantong 226010 Jiangsu, China;* ⓘ orcid.org/0000-0001-6046-063X; Email: ye_yu@pku.edu.cn

Authors

Pingfan Gu − *State Key Laboratory for Mesoscopic Physics, Nano-optoelectronics Frontier Center of the Ministry of Education, School of Physics, Peking University, Beijing 100871, China*

Yujia Sun − *State Key Laboratory of Superlattices and Microstructures, Institute of Semiconductors, Chinese Academy of Sciences, Beijing 100083, China; Center of Materials Science and Optoelectronics Engineering, University of Chinese Academy of Sciences, Beijing 100049, China*

Cong Wang − *Department of Physics and Beijing Key Laboratory of Optoelectronic Functional Materials and Micro-Nano Devices, Renmin University of China, Beijing 100872, China*

Yuxuan Peng − *State Key Laboratory for Mesoscopic Physics, Nano-optoelectronics Frontier Center of the Ministry of Education, School of Physics, Peking University, Beijing 100871, China;* ⓘ orcid.org/0000-0002-8009-8532

Yaozheng Zhu − *State Key Laboratory for Mesoscopic Physics, Nano-optoelectronics Frontier Center of the Ministry of Education, School of Physics, Peking University, Beijing 100871, China*

Xing Cheng − *State Key Laboratory for Mesoscopic Physics, Nano-optoelectronics Frontier Center of the Ministry of Education, School of Physics, Peking University, Beijing 100871, China*

Kai Yuan − *State Key Laboratory for Mesoscopic Physics, Nano-optoelectronics Frontier Center of the Ministry of Education, School of Physics, Peking University, Beijing 100871, China*

Chao Lyu − *State Key Laboratory for Mesoscopic Physics, Nano-optoelectronics Frontier Center of the Ministry of Education, School of Physics, Peking University, Beijing 100871, China*

Xuelu Liu − *State Key Laboratory of Superlattices and Microstructures, Institute of Semiconductors, Chinese Academy of Sciences, Beijing 100083, China*

Qinghai Tan − *State Key Laboratory of Superlattices and Microstructures, Institute of Semiconductors, Chinese Academy of Sciences, Beijing 100083, China;* ⓘ orcid.org/0000-0003-4808-4795

Qinghua Zhang − *Beijing National Laboratory for Condensed Matter Physics, Institute of Physics, Chinese Academy of Sciences, Beijing 100190, China*

Lin Gu − *Beijing National Laboratory for Condensed Matter Physics, Institute of Physics, Chinese Academy of Sciences, Beijing 100190, China;* ⓘ orcid.org/0000-0002-7504-031X

Zhi Wang − *Shenyang National Laboratory for Materials Science, Institute of Metal Research, Chinese Academy of Sciences, Shenyang 110016, China*

Hanwen Wang − *Shenyang National Laboratory for Materials Science, Institute of Metal Research, Chinese Academy of Sciences, Shenyang 110016, China*

Kenji Watanabe − *Research Center for Functional Materials, National Institute for Materials Science, Tsukuba 305-0044, Japan;* ⊙ orcid.org/0000-0003-3701-8119

Takashi Taniguchi − *International Center for Materials Nanoarchitectonics, National Institute for Materials Science, Tsukuba 305-0044, Japan;* ⊙ orcid.org/0000-0002-1467-3105

Jinbo Yang − *State Key Laboratory for Mesoscopic Physics, Nano-optoelectronics Frontier Center of the Ministry of Education, School of Physics, Peking University, Beijing 100871, China;* ⊙ orcid.org/0000-0003-3517-9701

Ping-Heng Tan − *State Key Laboratory of Superlattices and Microstructures, Institute of Semiconductors, Chinese Academy of Sciences, Beijing 100083, China; Center of Materials Science and Optoelectronics Engineering, University of Chinese Academy of Sciences, Beijing 100049, China;* ⊙ orcid.org/0000-0001-6575-1516

Complete contact information is available at:
https://pubs.acs.org/10.1021/acs.nanolett.1c04373

Author Contributions

●P.G., Y.S., and C.W. contributed equally to this work.

Author Contributions

Y.Y. and P.G. conceived the project. P.G., K.Y., and Y.P. synthesized the crystals. P.G., K.Y., H.W., and C.L. fabricated the devices. Y.S., X.L., and Q.T. conducted the Raman measurements under the supervision of J.Z. and P.T. C.W. conducted the DFT calculation under the supervision of W.J. Y.P. conducted the VSM measurements under the supervision of J.Y. Y.Z. and P.G. conducted the analytical theory. X.C. collected the magnet-optical images. Z.W. conducted the MFM measurements under the supervision of Z.H. P.G. performed the electrical transport measurements, heat capacity measurements and analyzed the data. K.W. and T.T. grew the hBN bulk crystals. P.G. and Y.Y. drafted the manuscript. All authors discussed the results and contributed to the manuscript.

Notes

The authors declare no competing financial interest.

■ REFERENCES
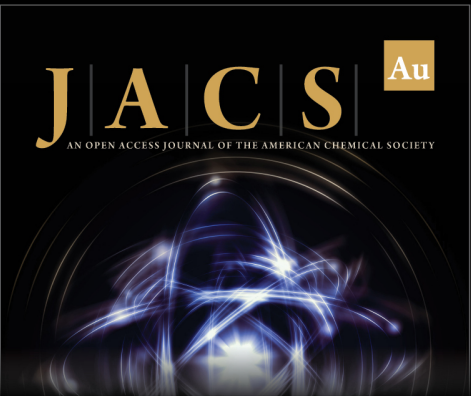
(1) Grüner, G. The dynamics of charge-density waves. *Rev. Mod. Phys.* **1988**, *60*, 1129.

(2) Grüner, G. The dynamics of spin-density waves. *Rev. Mod. Phys.* **1994**, *66*, 1.

(3) Bray, J.; et al. Observation of a spin-Peierls transition in a Heisenberg antiferromagnetic linear-chain system. *Phys. Rev. Lett.* **1975**, *35*, 744.

(4) Cheong, S.-W.; Mostovoy, M. Multiferroics: a magnetic twist for ferroelectricity. *Nat. Mater.* **2007**, *6*, 13−20.

(5) Krimmel, A.; et al. Incommensurate structure of the spin-Peierls compound TiOCl in zero and finite magnetic fields. *Phys. Rev. B* **2006**, *73*, 172413.

(6) Schönleber, A.; van Smaalen, S.; Palatinus, L. Structure of the incommensurate phase of the quantum magnet TiOCl. *Phys. Rev. B* **2006**, *73*, 214410.

(7) van Smaalen, S.; Palatinus, L.; Schönleber, A. Incommensurate interactions and nonconventional spin-Peierls transition in TiOBr. *Phys. Rev. B* **2005**, *72*, 020105.

(8) Zhang, T.; et al. Magnetism and optical anisotropy in van der Waals antiferromagnetic insulator CrOCl. *ACS Nano* **2019**, *13*, 11353−11362.

(9) Wang, M.; et al. Broadband CrOCl saturable absorber with a spectral region extension to 10.6 μm. *Adv. Opt. Mater.* **2020**, *8*, 1901446.

(10) Forsberg, H.-E.; Songstad, J.; Viljanto, J.; Seppala, P.; Theander, O.; Flood, H. On the structure of CrOCl. *Acta Chem. Scand.* **1962**, *16*, 777.

(11) Noerlund Christensen, A.; Johansson, T.; Quézel, S. Preparation and Magnetic Properties of CrOCl. *Acta Chem. Scand. A* **1975**, *6*, 1171−1174.

(12) Coic, L.; Spiesser, M.; Palvadeau, P.; Rouxel, J. Chromium (III) oxyhalides: Magnetic and optical properties. Lithium intercalation. *Mater. Res. Bull.* **1981**, *16*, 229−236.

(13) Reuvekamp, P. G. Investigation into the magnetic and the structural properties of two low-dimensional antiferromagnets $TiPO_4$ and CrOCl. Ph.D. Thesis, University of Stuttgart, Stuttgart, Germany, 2014.

(14) Zhang, J. Temperature dependent magnetic order in FeOCl type compounds. Ph.D. Thesis, University of Bayreuth, Bayreuth, Germany 2014.

(15) Angelkort, J.; Wölfel, A.; Schönleber, A.; van Smaalen, S.; Kremer, R. K. Observation of strong magnetoelastic coupling in a first-order phase transition of CrOCl. *Phys. Rev. B* **2009**, *80*, 144416.

(16) Wang, Z.; et al. Determining the phase diagram of atomically thin layered antiferromagnet $CrCl_3$. *Nat. Nanotechnol.* **2019**, *14*, 1116−1122.

(17) Peng, Y.; et al. Magnetic structure and metamagnetic transitions in the van der Waals antiferromagnet $CrPS_4$. *Adv. Mater.* **2020**, *32*, 2001200.

(18) Zhang, F.; et al. Super-exchange theory for polyvalent anion magnets. *New J. Phys.* **2019**, *21*, 053033.

(19) Miao, N.; Xu, B.; Zhu, L.; Zhou, J.; Sun, Z. 2D intrinsic ferromagnets from van der Waals antiferromagnets. *J. Am. Chem. Soc.* **2018**, *140*, 2417−2420.

(20) Bykov, M.; Bykova, E.; Dubrovinsky, L.; Hanfland, M.; Liermann, H.-P.; van Smaalen, S. Pressure-induced normal-incommensurate and incommensurate-commensurate phase transitions in CrOCl. *Sci. Rep.* **2015**, *5*, 1−5.

(21) Wang, C.; et al. A family of high-temperature ferromagnetic monolayers with locked spin-dichroism-mobility anisotropy: MnNX and CrCX (X= Cl, Br, I; C= S, Se, Te). *Sci. Bull.* **2019**, *64*, 293−300.

(22) Rong, Q.-Y.; Hu, A.-M.; Zhang, X.-H.; Wang, L.-L.; Xiao, W.-Z. Ferromagnetism and controllable half-metallicity of two-dimensional hexagonal CrOX (X= F, Cl, Br) monolayers. *J. Magn. Magn. Mater.* **2020**, *515*, 167310.

(23) Qing, X.; et al. Magnetism and spin exchange coupling in strained monolayer CrOCl. *Phys. Chem. Chem. Phys.* **2020**, *22*, 17255−17262.

(24) Nair, A.; Rani, S.; Kamalakar, M. V.; Ray, S. J. Bi-stimuli assisted engineering and control of magnetic phase in monolayer CrOCl. *Phys. Chem. Chem. Phys.* **2020**, *22*, 12806−12813.

(25) Jang, S. W.; et al. Hund's physics and the magnetic ground state of CrOX (X= Cl, Br). *Phys. Rev. Mater.* **2021**, *5*, 034409.

(26) Xu, C.; et al. A first-principles study on the electronic property and magnetic anisotropy of ferromagnetic CrOF and CrOCl monolayers. *J. Phys.: Condens. Matter* **2021**, *33*, 195804.

(27) Li, S.; et al. First-order magnetic and structural phase transitions in $Fe_{1+y} Se_x Te_{1−x}$. *Phys. Rev. B* **2009**, *79*, 054503.

(28) Fausti, D.; et al. Symmetry disquisition on the TiOX phase diagram (X= Br, Cl). *Phys. Rev. B* **2007**, *75*, 245114.

(29) Tian, Y.; Gray, M. J.; Ji, H.; Cava, R.; Burch, K. S. Magneto-elastic coupling in a potential ferromagnetic 2D atomic crystal. *2D Mater.* **2016**, *3*, 025035.

(30) Milosavljević, A.; et al. Evidence of spin-phonon coupling in $CrSiTe_3$. *Phys. Rev. B* **2018**, *98*, 104306.

(31) Du, L.; et al. Lattice dynamics, phonon chirality, and spin-phonon coupling in 2D itinerant ferromagnet Fe_3GeTe_2. *Adv. Funct. Mater.* **2019**, *29*, 1904734.

(32) Kozlenko, D. P.; Lis, O. N.; Kichanov, S. E.; Lukin, E. V.; Belozerova, N. M.; Savenko, B. N. Spin-induced negative thermal expansion and spin-phonon coupling in van der Waals material $CrBr_3$. *npj Quantum Mater.* **2021**, *6*, 1−5.

(33) Lee, J.-U.; et al. Ising-type magnetic ordering in atomically thin $FePS_3$. *Nano Lett.* **2016**, *16*, 7433−7438.

(34) Long, G.; et al. Persistence of magnetism in atomically thin $MnPS_3$ crystals. *Nano Lett.* **2020**, *20*, 2452−2459.

(35) Lenzlinger, M.; Snow, E. Fowler-nordheim tunneling into thermally grown SiO_2. *J. Appl. Phys.* **1969**, *40*, 278−283.

(36) Simmons, J. G. Generalized formula for the electric tunnel effect between similar electrodes separated by a thin insulating film. *J. Appl. Phys.* **1963**, *34*, 1793−1803.

(37) Wang, S.; Wahiduzzaman, M.; Davis, L.; Tissot, A.; Shepard, W.; Marrot, J.; Martineau-Corcos, C.; Hamdane, D.; Maurin, G.; Devautour-Vinot, S.; Serre, C. Very large tunneling magnetoresistance in layered magnetic semiconductor CrI_3. *Nat. Commun.* **2018**, *9*, 1−8.